ACS EARTH AND SPACE CHEMISTRY

http://pubs.acs.org/journal/aesccq

Article

Sulfide Immobilization: Investigating the Impact of a Protective Sulfide-Bearing Layer Formed by Siderite ($FeCO_3$)

Spencer D. Bingham, Alon V. McCormick, and R. Lee Penn*

Cite This: *ACS Earth Space Chem.* 2023, 7, 1247−1257

Read Online

ACCESS | Metrics & More | Article Recommendations | Supporting Information

ABSTRACT: Sulfate-rich wastewater poses ecological hazards to freshwater ecosystems, and sulfate is highly regulated in many Minnesota lakes. Biological sulfate reduction results in the reduction of sulfate to sulfide, and this process is used to remediate acid mine drainage. Theoretically, the aqueous sulfide can be immobilized into a solid-phase material and removed from the aqueous system. This study focuses on sulfide immobilization using iron-bearing waste minerals. Specifically, the extent of reaction of siderite ($FeCO_3$), an abundant ferrous mineral in some mining wastes, with sulfide was studied. Mildly acidic batch reactors containing powdered siderite were consecutively injected with a sodium sulfide solution. Solid reaction products were identified and characterized using powder X-ray diffraction, scanning and transmission electron microscopy, and energy-dispersive X-ray spectroscopy. Mackinawite (FeS) appeared to be the most abundant product, with greigite (Fe_3S_4) also detected. Results reveal that the immobilization capacity of sulfide by siderite is limited by the concentration of the Fe^{2+}(aq) presented in the system immediately before the initial sulfide exposure as the Fe^{2+}(aq) levels are not replenished after sulfidation. These results improve our understanding of the sulfidation of siderite and provide insight to improve the viability of using siderite-containing mining waste rock in a sulfate remediation technology.

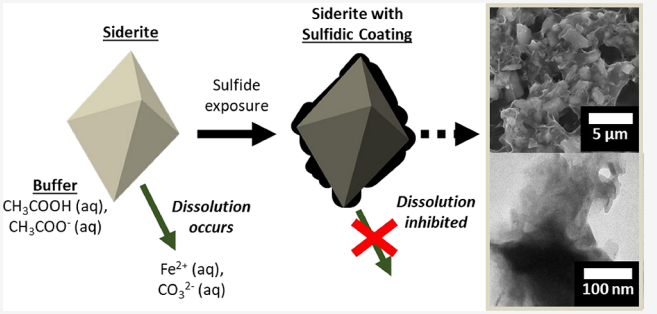

KEYWORDS: *siderite, sulfide immobilization, iron sulfide, mackinawite, coatings, environmental nanoparticles*

INTRODUCTION

Sulfate (SO_4^{2-}) is a common anion in natural waters and also a byproduct of the paper and food processing industries and extractive industries like coal and mineral mining.[1−6] High concentrations of sulfate can cause negative impacts on the environment and human health. For example, acid mine drainage (AMD) is a specific kind of sulfate-containing aqueous waste often produced by mining activities and is a historical and persistent environmental concern.[4,7−10] AMD is very high in sulfate, in some cases up to 1700 mg/L,[11] and acidic, with pH values that typically range from 2 to 6,[7,12,13] though in extreme cases, they can even be negative.[14] These pH conditions mobilize heavy metals, posing additional environmental toxicity concerns.[4,12−14] In addition, high concentrations of sulfate have the potential to induce leaching of hazardous metals, such as Cu, Pb, and Cr, from pipes and other infrastructure.[15]

Existing AMD treatment methods prioritize increasing pH and immobilizing heavy metals and are typically optimized for the removal of sulfate.[11,16−19] Due to its limited adverse health impacts even at relatively high concentrations, the U.S. Environmental Protection Agency recommends that the sulfate level in drinking water should not exceed 250 mg/L, as a guideline.[20] However, individual states can set more stringent regulations.

In the state of Minnesota, sulfate concentrations in lakes where manoomin (the Ojibwe term for wild rice, *Zizania palustris*) grows cannot exceed 10 mg/L.[21] This limit is based on evidence that sulfate contamination is severely detrimental to the health of the manoomin.[22] This lower sulfate limit is a legislated and treaty-protected requirement to protect the manoomin plant.[21,23,24] Minnesota is also home to the Mesabi Iron Range, a productive region for iron mining and a source of sulfate contamination into wild rice lakes[25] and home to the Duluth Complex, an undeveloped region east of the Mesabi Range enriched in Cu, Ni, and Pt-group elements.[26] If the Duluth Complex is developed for mineral extraction, it has the potential to contribute significantly to sulfate contamination.[27] These factors, given expected increases in domestic mining

Received: March 28, 2023
Revised: May 15, 2023
Accepted: May 17, 2023
Published: June 2, 2023

https://doi.org/10.1021/acsearthspacechem.3c00080
ACS Earth Space Chem. 2023, 7, 1247−1257

activities,[28−31] necessitate better strategies to treat sulfate-contaminated waters.

Biological sulfate reduction (BSR) reactors contain sulfate-reducing bacteria (SRB) that reduce sulfate to sulfide. BRS reactors have been well-investigated and are promising for treatment of high-sulfate water.[32] The immobilization of the sulfide produced, however, has not been studied as thoroughly and is essential to closing the loop between sulfate remediation from contaminated water and preventing subsequent release (or re-release) of sulfur species into nearby fresh water sources (e.g., lakes, rivers, groundwater). Typically, the sulfide produced in the BSR reactor is outgassed,[32,33] partially oxidized to form elemental sulfur,[34−36] or precipitated with Fe ions in a permeable reactive barrier.[37,38] Sometimes, a single substrate (straw, manure, woodchips, etc.) is chosen for concurrent sulfate reduction and sulfide immobilization. This material can serve as both a food source for the SRB and an adsorbent or source of metal ions, leading to precipitation of metal sulfides.[39] Several waste streams have been investigated for use as sulfide immobilizers, including agricultural waste,[40,41] sewage sludge,[42] and even wastes from sodium (bi)carbonate production.[43]

It is often helpful to examine valorizable waste streams located near areas with sulfate contamination. Recovery and use of otherwise low-value or valueless resources from local waste streams could facilitate the reduction of sulfate contamination in the surrounding environment.[44−46] Rock wastes from mining in the Mesabi Range in Minnesota contain appreciable amounts of iron oxides, carbonates, and silicates.[47] These abundant waste minerals have little economic value but are promising for immobilization of the sulfide produced from BSR reactors, thereby treating local sulfate-contaminated waters using local, solid wastes. For the iron-bearing minerals within the wastes to be chemically accessible, the rock must be pulverized; this already occurs at various points in mineral processing or via waste beneficiation processes (e.g., road construction).[48,49] This pollution remediation strategy would advance a circular economy and is in line with green chemistry and sustainable engineering principles.[50−52]

Siderite ($FeCO_3$) is commonly observed in the rock wastes of iron mining in Minnesota,[47,53] and it is a useful source of iron for sulfide immobilization due to the +2 oxidation state of iron. Additionally, the process of mineral dissolution releases carbonate ions, which have acid buffering capacity. This buffering capacity can help neutralize acid in the process water or generated during the anaerobic sulfate remediation process, which could further minimize the potential negative impacts on the surrounding environment. Other iron-bearing minerals identified in local rock wastes include ferric (oxyhydr)oxides such as goethite and hematite and the mixed valence iron oxide magnetite.

The sulfidation of ferric minerals has been studied extensively and has been shown to largely produce elemental sulfur.[54−57] There has been some study on the sulfidation of siderite with concentrations of sulfide in far excess of iron, showing the formation of smythite (Fe_9S_{11}), with some mackinawite (FeS) observed as well.[58,59] However, these studies do not necessarily represent the chemical conditions expected when effluent from a BSR reactor, with sulfide concentrations on the order of a few mM,[32,60] encounters Fe-bearing minerals, with iron far in excess of the sulfide. Previous research on the sulfidation of iron-bearing mineral mixtures for this application revealed that the mineralogy of rock wastes plays a significant role in the immobilization rate.[49] Further, materials containing siderite show promise for sulfide immobilization due to the faster reaction rate with and higher capacity of siderite as compared to other iron-bearing minerals.[61] However, as only mineral mixtures were assessed, the contribution of siderite to the overall sulfide immobilization capacity has not been quantified, and the products of siderite sulfidation have not been independently characterized.

A system related to the sulfidation of siderite, where a source of Fe^{2+} is in excess relative to sulfide, is that of sulfidic steel corrosion. In a sulfidic, reducing environment, steels release Fe^{2+}, which reacts with sulfide to form a "protective layer" over the steel surface that prevent future corrosion until the layer cracks, flakes, or spalls.[62−66] When zero-valent iron particles are sulfidated, well-defined, thin shells of mackinawite are formed around the Fe particles, and these thin shells persist for several months.[67] For the sulfidation of siderite, if an analogous protective coating of mackinawite forms on the siderite particles, the capacity of the siderite to immobilize aqueous sulfide is hypothesized to decrease as compared to thermodynamic predictions due to loss of direct contact between the siderite and the aqueous environment, resulting in substantially lower Fe^{2+}(aq) concentrations and thus limiting precipitation of iron sulfides. Here, the sulfidation of siderite was assessed in mildly acidic conditions designed to more closely represent pH conditions typical of BSR reactor effluent[32,68−70] and when the Fe^{2+} source, siderite, is in excess relative to the sulfide introduced.

MATERIALS AND METHODS

Sulfidation and Aqueous Analysis. All experiments were performed in an anaerobic glovebag (95% N_2, 5% H_2; Coy Laboratory Products) using N_2-purged, ultrapure 18.2 MΩ·cm water from a MilliPore Milli-Q Advantage A10 system that has been equilibrated anaerobically overnight. Experiments were performed when gaseous oxygen concentrations were below 1 ppm. Siderite (Ward's Science; Antigonish County, Nova Scotia, Canada; Lot 502748; Fe:Mn ≈ 5:1) was ground into a fine powder using a mortar and pestle. Optical analysis showed shard-like granules with a modal diameter of approximately 1.4 μm, though the larger particles, while fewer in number, contributed most to the mass of siderite in the reactors (Figure S1). Compositional analysis was done using inductively coupled plasma−optical emission spectroscopy (ICP-OES) following existing methods, described in the SI.[71] Batch reactors were prepared by adding siderite powder into 37 mL serum bottles equipped with a magnetic stir bar.

The bottles were filled with a 10 mM acetic acid buffer adjusted to pH 4.7 with 1 M HCl or 0.5 M NaOH. This pH value was chosen to mimic the effluent of a BSR reactor, which tends to be higher than the BSR feed due to oxidation of organic matter to acetate and carbonate during sulfate reduction (thus, better modeling conditions for subsequent sulfide immobilization).[32,72,73] The bottles were filled to the point of no headspace and crimp-capped to prevent the evolution of H_2S(g) and CO_2(g). Reactors were stirred at 500 rpm and allowed to equilibrate for 7 days prior to sulfide exposure.

Aqueous solutions of HCl and NaOH, which were used for pH adjustments, were prepared using concentrated solutions of HCl (BDH Aristar, 12.1 M, 36.5−38.0%) and NaOH (Fisher Scientific, 19 M, 50% w/w). A stock solution of 500 ppm sulfide ($Na_2S{\cdot}9H_2O$, >98%, Sigma Aldrich) was freshly

https://doi.org/10.1021/acsearthspacechem.3c00080
ACS Earth Space Chem. 2023, 7, 1247−1257

prepared in the glovebag before each sulfidation reaction. Hydrogen sulfide gas evolution posed a potential safety hazard: The gas was immobilized within the glovebag by a silver nitrate trap.[74] Sulfidation reactions were initiated by using a constant-volume sampling method to maintain the closed and headspace-free condition of each reactor and is described in the Supporting Information (SI). The excess volume from constant-volume spiking was saved for quantifying the Fe^{2+}(aq) and sulfide concentrations at the moment of sulfide exposure. An Orion PerpHecT ROSS Combination pH Micro Electrode and a VWR sympHony B10P meter were used to measure the pH of the remaining filtrate.

The samples were filtered (Agilent 0.2 μm, 13 mm, nylon) before preparation for UV−Vis analysis. The ferrozine (3-(2-pyridyl)-5,6-diphenyl-1,2,4-triazine-*p*,*p*′-disulfonic acid monosodium salt hydrate, Sigma-Aldrich 97%) assay was used to quantify Fe^{2+}(aq).[75] For quantifying sulfide concentrations, Hach Method 3181 was modified to accommodate small sample volumes, with 50 μL of Sulfide Reagents 1 and 2 (Hach, cat. 181632 and 131732) each per 3 mL of total volume.[76] Absorbance measurements were performed using an Agilent 8453 UV−Vis spectrometer equipped with tungsten and deuterium lamps.

Post-spike aqueous analysis experiments used the following parameters: Each reactor contained approximately 75 mg of siderite and was assigned a number of sulfide spikes it would receive before being monitored for sulfide and Fe^{2+}(aq) concentrations and pH (Blank − No sulfide, Sample 1−1 spike, Sample 2−2 spikes, etc.). The reactors were all spiked with 1 mL of 500 ppm sulfide on a weekly basis to allow for re-equilibration. Beginning after the last spike for a given reactor, samples for Fe^{2+}(aq) and sulfide quantification and pH measurement were obtained by constant-volume exchange of the acetate buffer and reactor contents at 5 min and 1 day after the final sulfide spike and then weekly thereafter (Table S1).

Sulfide immobilization capacity experiments used several different starting mass loadings of siderite, with each reactor spiked with the sulfide stock solution at an interval of at least 90 min between spikes. The timing of sulfide spikes was chosen after analysis of the results in Figure 1. The mass ratio of siderite to sulfide contained in each spike volume ranged from 150 to 2000. Sulfide immobilization capacity was determined to be reached when the Fe^{2+}(aq) concentration was less than 0.1 mM and aqueous sulfide became detectable with an additional spike.

Visual MINTEQ (ver. 3.1) was used to determine the concentrations of iron and sulfur species at equilibrium as a function of sulfide addition for reaction conditions used in this work, with details provided in the SI.

Solid-Phase Characterization. Post-reaction solids were collected and washed thrice by centrifugation (Eppendorf 5804) and re-dispersal in deoxygenated, ultrapure water in the glovebag followed by drying in the glovebag or under a stream of nitrogen.

X-ray diffraction was performed using a Panalytical X'Pert PRO X-ray diffractometer equipped with a cobalt source (1.7909 Å) and an X'Celerator line detector. When necessary, oxidation could be slowed by preparation of the samples using a sample holder equipped with a plastic dome (Malvern Panalytical Pro. No. 9430 500 29101) in the glovebag. An XRD pattern was collected using this sample holder prior to sample loading, and significant background signal was observed. This background signal was manually subtracted from the XRD pattern collected for each sample.

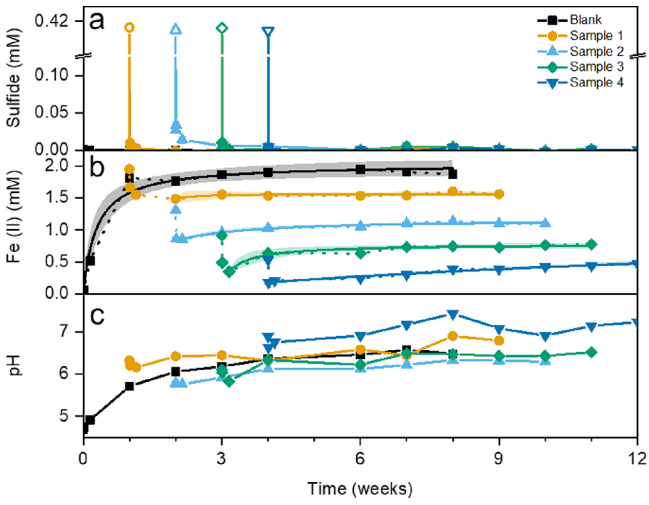

Figure 1. Plot of concentration of aqueous sulfide (a) and Fe^{2+}(aq) (b) and pH (c) over time in the blank and Samples 1−4, with the sample number representing the number of spikes that reactor received. Connecting lines serve to guide the eye only. Open points in panel (a) indicate calculated values from known sulfide spike concentrations and any remaining quantifiable sulfide in solution from previous spikes. In panel (b), dashed lines are meant to guide the eye, solid lines indicate fitted results, and shaded regions are the associated 95% confidence intervals of the fit.

Transmission electron microscopy (TEM) imaging was performed using an FEI Tecnai T12 operating at an accelerating voltage of 120 kV. Lattice fringe analysis was performed using ImageJ.[77] Scanning electron microscopy (SEM) imaging was performed using a JEOL JSM-6010PLUS/LA equipped with an integrated energy dispersive spectroscopy (EDS) detector. EDS analysis was performed with the InTouchScope software.

RESULTS AND DISCUSSION

Sulfide Immobilization by Rapid Precipitation with Fe^{2+}(aq). Prior to the addition of sulfide, the contents of each reactor initially appeared cloudy white due to the presence of the suspended siderite particles. As soon as the first sulfide spike was delivered, the suspension in each reactor darkened to a gray black. Additional spikes did not visibly darken the reactors further, and the blank reactor remained cloudy white for the duration of the experiment. Visually, this observation was consistent with the formation of iron sulfides, which are black.[78−80]

The addition of sulfide to the aqueous suspension of siderite resulted in a rapid decrease of the aqueous sulfide concentration to very low or undetectable levels within minutes, with stochiometric drops in Fe^{2+}(aq) concentration. Figure 1 shows evolving sulfide and Fe^{2+}(aq) concentrations and pH in siderite-containing reactors over time and over several sulfide spikes. The concentration of aqueous sulfide in Samples 1−4 rapidly decreased to below quantifiable levels within minutes of sulfidation (Figure 1a). Though constant-volume spiking sequentially diluted the sample by approximately 3% per spike, the rapid decline in aqueous sulfide concentration within minutes after spiking rendered it unnecessary to adjust reported concentrations as no detectable sulfide remained in the reactors by the time the next sulfide

https://doi.org/10.1021/acsearthspacechem.3c00080
ACS Earth Space Chem. 2023, 7, 1247−1257

spike took place. Sulfide concentrations remained undetectable for the duration of the experiment and after multiple spikes, indicating that sulfide had been effectively immobilized and removed from the aqueous phase. No sulfide was detected in the blank reactor, which is as expected.

The drop in sulfide concentration was accompanied by an approximately equimolar drop in $Fe^{2+}(aq)$ (Figure 1b). This result is consistent with the rapid precipitation of an iron monosulfide, FeS.[54,78,81,82] After the sulfide concentration dropped to below detection levels, the $Fe^{2+}(aq)$ concentrations did not rebound to the pre-spike, equilibrium values even though the concentration remained lower than the concentration expected with siderite present throughout the experiments (Figure S2). It should be noted that after 7 days of equilibration, weekly measurements of the $Fe^{2+}(aq)$ concentration in the non-sulfidated reactor remained within 5% of an average value (Figure 1b), and therefore 1 week was considered an appropriate time for equilibration prior to and between spikes.

The pH values increased to higher than the initial 4.7 value (Figure 1c), which is consistent with the dissolution of the siderite during the week-long equilibration prior to any sulfidation. The blank reactor shows that the increase in pH follows the increase in $Fe^{2+}(aq)$ concentration due to the concurrent release of carbonate ions and ferrous ions. Sulfidated samples had pH values that stayed fairly constant with time, in the range 6.3−7.5. The overall increase in pH values appears independent of sulfidation. However, within 5 min of a sulfide spikes, Samples 1−4 show short-term small increases in pH that then return to lower values. This result is likely caused by the rapid protonation of the injected sulfide to form bisulfide followed by release of that proton when the sulfide precipitates with aqueous Fe^{2+} as FeS. The net proposed reaction of the system (eq 1) shows the release of carbonate, which will act as a weak base to increase pH (Figure 1).

$$FeCO_3 + HS^{2-} \rightarrow FeS + HCO_3^{2-} \quad (1)$$

The source of $Fe^{2+}(aq)$ before sulfidation is siderite, and due to its considerably higher solubility than the iron sulfides under these pH conditions,[54,78,83−86] siderite remains the source of soluble Fe^{2+} during these experiments. The rate at which $Fe^{2+}(aq)$ increases after sulfidation, and therefore the rate of siderite dissolution changed after the first sulfidation. In the non-sulfidated, blank sample, the $Fe^{2+}(aq)$ data showed an increase before leveling off to a steady-state value. Sulfidated samples had smaller increases in $Fe^{2+}(aq)$, reaching plateau moments after spiking.

The data were fit to a model to facilitate the quantitative comparison of siderite dissolution rates. To model these data, an equation of the form shown in Eq 2 was chosen due to its mathematical form: The slope is always positive given positive, non-zero A and B, in the limit of $x \rightarrow 0$, the slope of the function approaches the constant AB showing linear dissolution of the mineral, and as $x \rightarrow \infty$, the slope of the function approaches 0, indicating a steady-state. A linear dissolution rate was considered appropriate because the batch reactors were continuously stirring, putting the system in a surface-controlled regime where dissolution is proportional to the surface area of the mineral.[87,88]

$$y = \frac{ABx}{1 + Bx} \quad (2)$$

$$[Fe^{2+}(aq)] = \frac{[Fe^{2+}(aq)]_{max}\, Bt}{1 + Bt},\ k = B[Fe^{2+}(aq)]_{max} \quad (3)$$

After fitting the data in Figure 1A, three parameters were determined: $[Fe^{2+}(aq)]_{max}$, the steady-state $Fe^{2+}(aq)$ concentration as $t \rightarrow \infty$, B, a constant with units of $weeks^{-1}$ that describes the dependence of dissolution rate on $Fe^{2+}(aq)$ during the transition between linear dissolution and steady-state regimes, and k, the linear siderite dissolution rate with units of $mM{\cdot}weeks^{-1}$. The k values (Table S2) show that despite modest increases in $Fe^{2+}(aq)$ concentrations over time in Samples 1−4 after their final respective sulfide spikes, sulfidated mineral dissolution rates were 1−2 orders of magnitude lower than the blank.

These results indicate that after siderite was first exposed to sulfide in mildly acidic conditions, the dissolution rate slowed significantly, leading to a stepwise decline in $Fe^{2+}(aq)$ concentrations after each sulfide spike with only limited recovery of $Fe^{2+}(aq)$ between spikes. Because $Fe^{2+}(aq)$ concentrations fell stoichiometrically with sulfide and pH remained relatively constant after several sulfide spikes, immobilization appeared to occur primarily through precipitation of FeS in solution (eq 1). There seemed to be a limit on sulfide immobilization capacity that was not defined by thermodynamic arguments but rather by the amount of Fe^{2+} that was in solution before sulfide was first introduced.[89]

Modeling Results. The reactor chemistry was modeled using Visual MINTEQ to compare experimental results to thermodynamic expectations (Figure S2). The results indicate that, at thermodynamic equilibrium, siderite should react with sulfide to form mackinawite in a 1:1 stoichiometric relationship. Predicted capacity was defined by the amount of Fe^{2+} added in the form of siderite, and after capacity was reached, no solid siderite would remain, $Fe^{2+}(aq)$ concentrations would be vanishingly small, and aqueous sulfide concentrations would rise with any further spikes.

Experimentally, however, conversion of siderite to iron sulfide (predicted to be mackinawite) fell far short of the predicted conversion. Percent conversion values were 1−2 orders of magnitude lower than the 100% prediction by Visual MINTEQ. Further, $Fe^{2+}(aq)$ concentrations decreased with each spike and failed to rebound to predicted equilibrium values. These conflicts with model predictions indicate that there may be a barrier to siderite dissolution after the first sulfidation spike, leading to depressed $Fe^{2+}(aq)$ concentrations, and thus reduced capacity to immobilize sulfide within experimentally relevant and field-realistic time scales of minutes to weeks.

Characterization of Post-Reaction Solids. *X-ray Diffraction.* Powder XRD analysis of sulfidated siderite samples (Figure 2) showed the formation of mackinawite and, to a lesser extent, greigite ($Fe^{2+}Fe^{3+}{}_2S_4$). Three siderite reactors were prepared and spiked weekly with either 0, 5, or 8 sulfide spikes to achieve mass loadings of 0, 3.1, and 5.1% S (relative to the initial siderite added). Patterns were normalized to the most intense siderite peak at 37.3° 2θ.

Siderite was expected to be the most abundant phase present based on the stoichiometric limitation that no more than the amount of sulfide added can react to form an iron sulfide. Mackinawite was identified in both sulfidated samples by its characteristic peak at 20.3° 2θ corresponding to the (001) peak and the (101) peak at 35.0° 2θ. In the more sulfidated sample, the mackinawite peaks were more intense relative to

https://doi.org/10.1021/acsearthspacechem.3c00080
ACS Earth Space Chem. 2023, 7, 1247−1257

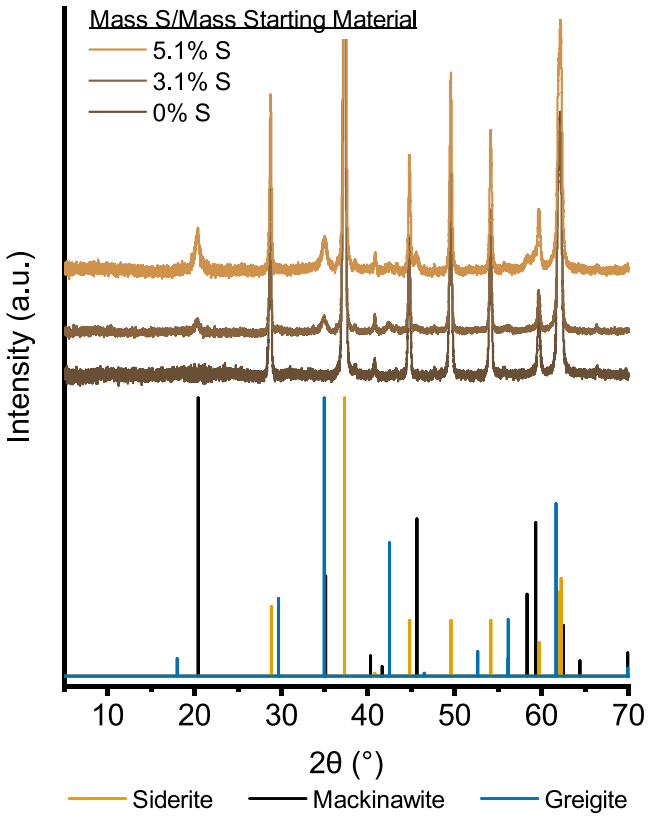

Figure 2. Diffraction patterns of sulfidated siderite. Stick patterns are siderite (00-029-0696), mackinawite (01-086-0389), and greigite (00-016-0713). The three samples are solids collected with no sulfide spiking or after sulfide spiking to achieve mass loadings of 3.1 or 5.1 mg S/mg siderite added.

the siderite and the 45.6°, 58.3°, and 59.3° 2θ mackinawite peaks became more apparent. The mackinawite 58.3° and 59.3° 2θ peaks were broad and quite close to the siderite 59.7° 2θ peak but were still resolvable. Despite significant overlap between the mackinawite and greigite peaks, the greigite peak at 42.5° 2θ does not overlap with either siderite or mackinawite, providing conclusive evidence that greigite formed. The presence of mackinawite was consistent with the MINTEQ predictions, but greigite was not predicted. Greigite is the primary oxidation product of mackinawite and forms via solid-phase transformation of mackinawite.[54,78,86,90−92] There was no clear oxidant in the system and the samples were not exposed to oxygen during concentration, washing, or XRD measurement. Considering reports of very high sensitivity of mackinawite to even trace oxygen,[93] the small amount of greigite observed by XRD is hypothesized to be a result of oxygen diffusion through the centrifuge tubes or domed XRD sample holder.

Scanning Electron Microscopy. Before exposure to sulfide, ICP-OES analysis yielded a siderite composition of $Mn_{0.12}Mg_{0.09}Fe_{0.76}CO_3$ and SEM-EDS analysis indicated the presence of each of these elements as well as Ca (detected but not quantifiable by ICP-OES (Figure 3d). The inclusion of Mn, Mg, and Ca is common in natural siderites, which form solid solutions with divalent cations depending on the conditions of their formation.[94]

After one sulfide spike, particles of siderite could still be clearly identified by their characteristic rhombohedral shape, but now an amorphous-looking flakey material also appeared to be attached to the siderite particles, as shown in Figure 3b. The flakey material appears less bright in the backscattered electron image, indicating that the material is either lower in density than the siderite or contains substantial void space, resulting in a net lower density and thus having a lower brightness. At higher magnification, the material appears both thin and folded (Figure 3c).

The EDS analysis of the post-sulfidation material exhibited peaks for the anticipated elements related to siderite; including

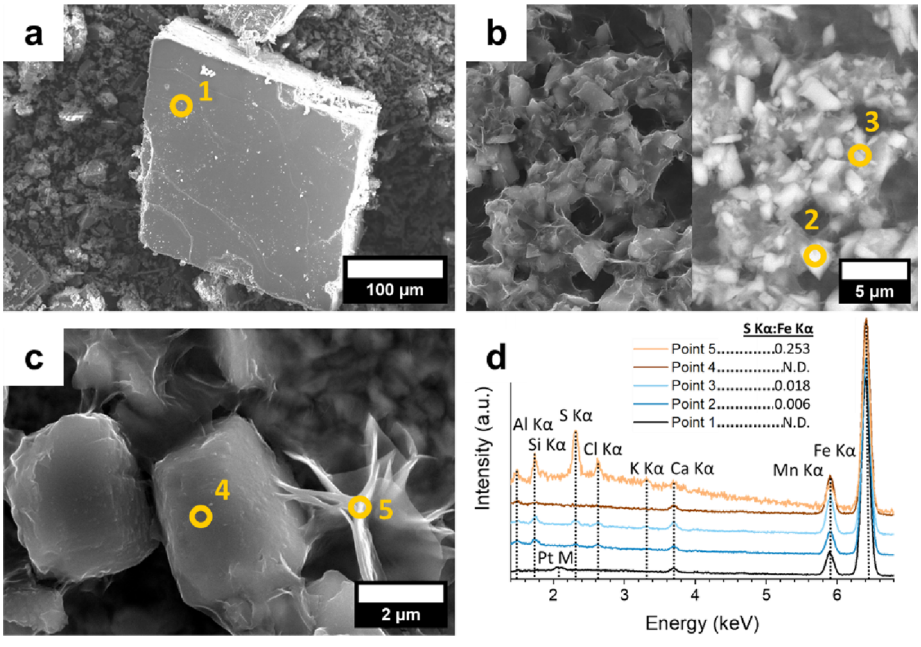

Figure 3. SEM images of (a) non-sulfidated siderite (platinum coated) (b, c) sulfidated siderite (carbon coated) and (d) associated EDS spectra. N.D. − not detected. Open circles indicate the location of the electron beam during analysis by EDS. All images are secondary electron images except (b, right), which is a backscattered electron image.

https://doi.org/10.1021/acsearthspacechem.3c00080
ACS Earth Space Chem. 2023, 7, 1247−1257

Fe, Ca, Mg, Mn, C, and O; along with the Na and Cl from the reaction buffer, and S. However, the EDS collected at point 5 in Figure 3c shows that this region has a higher S to Fe ratio but otherwise is compositionally similar to other parts of the sample. This indicates that individual siderite particles may have been entirely covered by the sheet-like material as seen by the semitransparency near the particle edges in Figure 3c. EDS analysis on point 4 did not show the presence of the S Kα peak; however, compositional analysis of this thin material may have been complicated by its sheer nature. The interaction volume of the 20 kV electron beam was expected to penetrate deeply into the sample (>2 μm).[95] This effect made characterization of a thin, protective coating of FeS over the siderite particles challenging using SEM-EDS.

Transmission Electron Microscopy. TEM analysis was used to characterize, at higher resolution, the morphology and crystallinity of the nanoparticles near the surface of the siderite particles. Crystalline nanoparticles with lattice spacings consistent with mackinawite and greigite were observed in sulfidated siderite samples (4% S) using high-resolution TEM (HRTEM). An integrated profile scan of the fringes in Figure 4b,c using ImageJ showed lattice fringes with spacings between

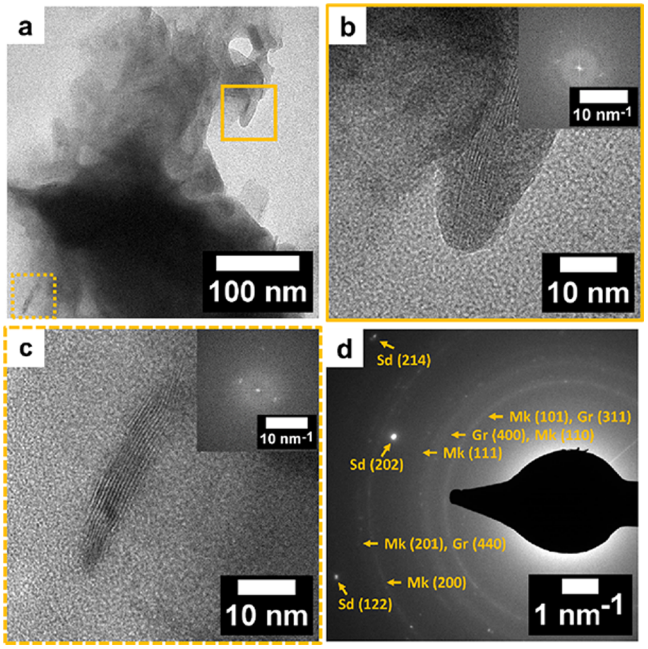

Figure 4. (a–c) TEM images of sulfidated siderite showing iron sulfide nanoparticles surrounding larger siderite particles. Insets: FFT of image showing frequencies associated with (b) the mackinawite (001) and greigite (220) planes and (c) the mackinawite (001) and (101) planes. (d) SAED pattern of panel (a) showing polycrystalline mackinawite (Mk) and greigite (Gr) and single crystals of siderite (Sd). For overlapping rings, lattice planes are ordered by increasing *d* spacing from left to right.

5 and 6 Å (Figures S3 and S4), corresponding to the (001) plane of mackinawite. While this range in spacing estimate was fairly large, the sheet-like nature of mackinawite allows for significant variability in the (001) spacing, which can hold intercalated species and can also relax over time.[96−98] The fast Fourier transform (FFT) of Figure 4b,c confirmed the lattice spacing for the (001) plane while also showing a spacing of 3.4 Å in Figure 4b and 2.9 Å in Figure 4c corresponding to the (220) plane of greigite and (101) plane of mackinawite, respectively. The observed sheetlike morphology was consistent with literature descriptions of flake-like particles of mackinawite.[96,98−101] The rhombohedral morphology of siderite was also consistently evident, but the siderite particles were not electron-transparent.

Nanoparticulate FeS Coating on Siderite Particles. The HRTEM micrographs, SEM images, compositional data, and XRD patterns are consistent with the formation of mackinawite and greigite nanoparticles that cover the siderite surfaces. These nanoparticles inhibit the reactivity of the siderite by forming a coating that encases the siderite, protecting it from the aqueous environment and preventing dissolution. Such protective barriers have been reported in the corrosion science community where reactions between steel and "sour," or H_2S-rich, oil and gas streams are of interest.[62−65,102] The primary difference between the sulfidation of siderite and steel is only that the neutral redox state of iron in steel requires oxidation to Fe^{2+} to react with sulfide to directly precipitate mackinawite. Otherwise, these are analogous processes, especially since the anoxic corrosion of steel occurs in an acid gas environment where CO_2 and H_2S can dissolve into the aqueous phase and liberate Fe^{2+} for reactions that form siderite and mackinawite, respectively.[62−65,102−104] This sulfidic tarnishing of steel forms a protective coating, inhibiting further reaction between the steel and the aqueous phase. These data tracking the sulfidation of siderite in mildly acidic conditions mimic the behavior of this sulfidic tarnishing of steel.

The observed decline in siderite reactivity, as seen in Figure 1, is consistent with the formation of a protective ion sulfide nanoparticulate coating. Further, because the sulfide immobilization capacity of siderite is mainly determined by the $Fe^{2+}(aq)$ concentration prior to sulfidation for precipitation as mackinawite and the protective layer prevents siderite dissolution to replenish $Fe^{2+}(aq)$, sulfide immobilization capacity is substantially reduced from the maximum stoichiometric prediction based on the initial siderite mass percent. Given that the inhibition of $Fe^{2+}(aq)$ regeneration is attributed to the protective coating of iron sulfide nanoparticles, it is possible to estimate the sulfide immobilization capacity by considering the available $Fe^{2+}(aq)$ and the number of sulfide spikes introduced into the system (as described in eq 4). Here, n represents the spike number and $[Fe^{2+}(aq)]_n$ represents the predicted $Fe^{2+}(aq)$ concentration in the reactor just before that sulfide spike. Plotting the data will reveal the number of spikes of a particular sulfide concentration that can be accommodated before all $Fe^{2+}(aq)$ is depleted, and the capacity is achieved at the x intercept. Equation 4 is valid as long as no rebound of dissolved $Fe^{2+}(aq)$ after each of the sulfidation spikes occurs.

$$[Fe^{2+}(aq)]_n = [Fe^{2+}(aq)]_0 - [Na_2S] \times (n - 1) \quad (4)$$

However, in some cases, some $Fe^{2+}(aq)$ rebound may occur. In the sulfidic corrosion of steels, the protective mackinawite layer was found to crack after reaching a critical thickness, and Shoesmith et al. specifically noted how these cracks would allow the release of soluble iron species, which could subsequently be precipitated as FeS.[64,102] The results presented in Figure 1 suggest that the effects of a protective mackinawite layer are similar. If the protective layer on the siderite cracked or was otherwise disrupted, the siderite surface would be re-exposed to the mildly acidic environment and allow for siderite dissolution, resulting in an increase in $Fe^{2+}(aq)$ concentrations. An experiment was performed that

https://doi.org/10.1021/acsearthspacechem.3c00080
ACS Earth Space Chem. 2023, 7, 1247−1257

assessed the sulfide immobilization capacity of siderite in reactors with a range of siderite mass loadings, where a proportionally lower siderite surface area would lead to proportionally thicker coatings, potentially allowing for cracking and re-release of $Fe^{2+}(aq)$.

Sulfide Immobilization Capacity of Siderite. Figure 5 is a series of plots showing $Fe^{2+}(aq)$ at the moment of each sulfide spike. The total sulfide immobilization capacity of siderite in acidic, buffered batch reactor conditions did not depend on the amount of sulfide present; instead, it appeared to depend entirely on the initial $Fe^{2+}(aq)$ concentration prior to sulfidation, which is in equilibrium with siderite and not dependent on mass loading while siderite is in excess. In Figure 5, data were not recorded between spikes, and reactors were spiked until sulfide immobilization capacity was met. Like in Figure 1, Figure 5 shows that, in most samples, $Fe^{2+}(aq)$ values do not rebound to the equilibrium value after initial decreases, but instead $Fe^{2+}(aq)$ values continued to fall with each sulfide spike (0.42 mM/spike) until immobilization capacity was reached (after 5−7 spikes). In fact, the $Fe^{2+}(aq)$ concentrations at a given spike could be predicted by eq 4.

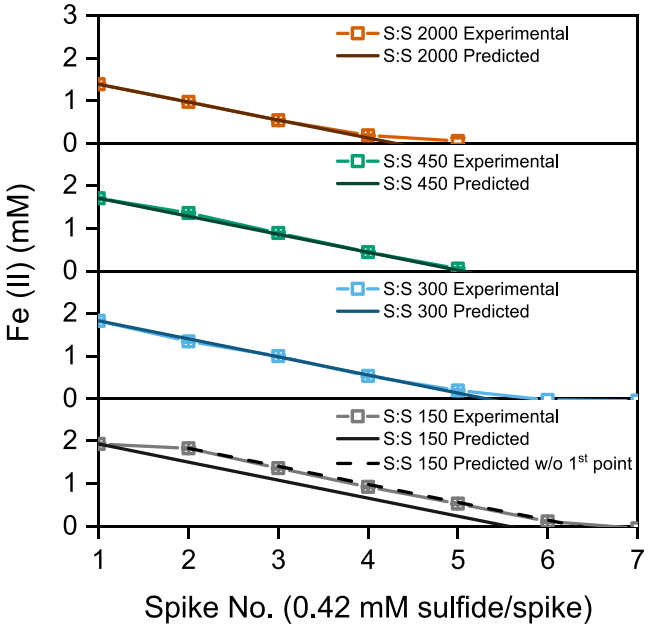

Figure 5. Experimental $Fe^{2+}(aq)$ concentrations (open squares) at the moment of spiking compared to predicted $Fe^{2+}(aq)$ concentrations assuming no siderite dissolution after exposure to sulfide. Lines connecting experimental data are meant to guide the eye only. S:S is the ratio of siderite added to the system to the mass of sulfide added per spike (ex. 150 mg of siderite with 0.5 mg S per spike is S:S 300).

The sulfide immobilization capacity, measured as the molar conversion of siderite to iron sulfide, observed in these experiments ranged from 1 to 16%. By solving for the x intercept (number of spikes), converting that number to a mass of sulfur, and dividing by the amount of siderite in the reactor, eq 4 accurately predicted the percentage of siderite conversion in samples with a siderite-to-sulfide ratio of 300 or greater.

In contrast, eq 4 did not accurately predict the percentage of siderite conversion for the reactor prepared with the lowest siderite to sulfide per spike ratio (S:S 150). In this reactor, which still had a large excess of siderite relative to added sulfide, $Fe^{2+}(aq)$ concentrations were observed to rebound after the first spike, but not after subsequent spikes. With the second spike and beyond, $Fe^{2+}(aq)$ declined stoichiometrically with added sulfide like the other reactors. When an identical experiment was performed but with half as much sulfide/spike (250 ppm vs 500 ppm) and similar siderite to sulfide/spike ratios (300 and 100), the same trends were observed: The sulfide immobilization capacity could be predicted to high accuracy with eq 4 and the lowest mass-loading sample had an $Fe^{2+}(aq)$ concentration that rebounded between the first and second spikes but not any time after (Figure S5). These results give evidence for a disruption in the iron sulfide nanoparticle coating that allowed for the dissolution of siderite to replenish $Fe^{2+}(aq)$. However, this effect only occurred between the first and second spikes, implying that the coating re-formed after the first spike, and after that, no fresh siderite was exposed.

The overall sulfide immobilization capacity was largely determined by the initial $Fe^{2+}(aq)$ concentration of the reactor prior to spiking. The total mass of added siderite was not a dominating factor for sulfide immobilization while siderite was in excess, since the $Fe^{2+}(aq)$ concentration is initially at the equilibrium solubility limit. In a situation where siderite is scarcer than what was assessed in these experiments, the mineral could completely dissolve prior to sulfidation, and the limited amount of dissolve Fe^{2+} initially in solution would provide an absolute limit to sulfide immobilization.

While sulfidated materials are expected to be sensitive to oxygen, evidence suggests that the formation of iron monosulfides is advantageous to prevent the re-release of sulfate upon oxidation.[92,105] There are both existing and proposed storage methods for oxygen-sensitive mineral mixtures.[106−108] The environmental weathering of these iron monosulfide-coated siderite particles is an interesting and necessary area of continued research.

CONCLUSIONS

Mackinawite has been predicted and observed to be a principal sulfide "sink" in sulfate remediation technologies that employ BSR.[37,38,60,109] While the argument of a 1:1 reaction of $Fe^{2+}(aq)$ with sulfide to FeS is accurate, sources of soluble Fe^{2+} may not be chemically accessible for sulfide immobilization in a deployed technology. Siderite, a promising sulfide-immobilizing material found in mining wastes due to the 2+ oxidation state of its Fe and high solubility in acidic conditions, may not fully convert to mackinawite in an aqueous system containing sulfide as thermodynamically predicted. The results indicate that only a small fraction of the iron bound within siderite is transformed into mackinawite. The formation of a thin, protective coating of mackinawite is hypothesized to suppress siderite dissolution rates over a timeframe of at least several weeks. Thus, the amount of sulfide that could be immobilized by siderite is limited by the formation of the coating; this limitation must be considered when relying on siderite as a primary source of ferrous ions.

These results have also shown that the fraction of siderite that participates in the immobilization is somewhat higher at lower mass loadings, perhaps due to early disruption of a relatively thicker protective coating that is susceptible to cracking. As the inevitable formation of a protective coating occurs, increasing mass loading leads to some reduction of total relative immobilization capacity. These results therefore can inform material selection and design decisions in a sulfate remediation technology that uses BSR coupled with sulfide

https://doi.org/10.1021/acsearthspacechem.3c00080
ACS Earth Space Chem. 2023, 7, 1247−1257

immobilization with siderite; they suggest that disrupting the protective coating may partially increase immobilization capacity. Finally, the continued development of this sulfate remediation strategy will require further study of the oxidation and weathering of these post-reaction, sulfidic, layered materials.

■ ASSOCIATED CONTENT

Supporting Information

The Supporting Information is available free of charge at https://pubs.acs.org/doi/10.1021/acsearthspacechem.3c00080.

Analytical procedures for optical granulometry, optical emission spectroscopy, and geochemical calculations; lattice fringe analysis; additional modeling results and replicate experiments (PDF)

■ AUTHOR INFORMATION

Corresponding Author

R. Lee Penn − *Department of Chemical Engineering and Materials Science, University of Minnesota, Twin Cities, Minneapolis, Minnesota 55455, United States;* orcid.org/0000-0002-9610-9507; Email: rleepenn@umn.edu

Authors

Spencer D. Bingham − *Department of Chemical Engineering and Materials Science, University of Minnesota, Twin Cities, Minneapolis, Minnesota 55455, United States;* orcid.org/0009-0004-0002-4122

Alon V. McCormick − *Department of Chemical Engineering and Materials Science, University of Minnesota, Twin Cities, Minneapolis, Minnesota 55455, United States;* orcid.org/0000-0002-8885-1330

Complete contact information is available at: https://pubs.acs.org/10.1021/acsearthspacechem.3c00080

Author Contributions

The manuscript was written through contributions of all authors. All authors have given approval to the final version of the manuscript.

Funding

This work was funded in part by MnDRIVE Environment and NSF Award No. 2237827.

Notes

The authors declare no competing financial interest.

■ ACKNOWLEDGMENTS

This material is based upon work supported by the National Science Foundation Graduate Research Fellowship Program under Grant No. 2237827. Any opinions, findings, and conclusions or recommendations expressed in this material are those of the author(s) and do not necessarily reflect the views of the National Science Foundation. This work was funded in part by the MnDRIVE Environment fund of the University of Minnesota. Parts of this work were carried out in the Characterization Facility, University of Minnesota, which receives partial support from the NSF through the MRSEC (Award Number DMR-2011401) and the NNCI (Award Number ECCS-2025124) programs.

■ REFERENCES

(1) Lens, P. N. L.; Visser, A.; Janssen, A. J. H.; Pol, L. W. H.; Lettinga, G. Biotechnological Treatment of Sulfate-Rich Wastewaters. *Crit. Rev. Environ. Sci. Technol.* **1998**, *28*, 41−88.

(2) Hubbe, M. A.; Metts, J. R.; Hermosilla, D.; Blanco, M. A.; Yerushalmi, L.; Haghighat, F.; Lindholm-Lehto, P.; Khodaparast, Z.; Kamali, M.; Elliott, A. Wastewater Treatment and Reclamation: A Review of Pulp and Paper Industry Practices and Opportunities. *BioRes* **2016**, *11*, 7953−8091.

(3) Chitapornpan, S.; Chiemchaisri, C.; Chiemchaisri, W.; Honda, R.; Yamamoto, K. Organic Carbon Recovery and Photosynthetic Bacteria Population in an Anaerobic Membrane Photo-Bioreactor Treating Food Processing Wastewater. *Bioresour. Technol.* **2013**, *141*, 65−74.

(4) Spitz, K.; Trudinger, J. *Mining and the Environment: From Ore to Metal*; 2019, DOI: 10.1201/9781351183666.

(5) Lottermoser, B. Mine Wastes: Characterization, Treatment, Environmental Impacts. *Choice Rev. Online* **2008**, *45*, 45-2630−45−2630.

(6) Gupta, A.; Sar, P. Treatment Options for Acid Mine Drainage: Remedial Achievements Through Microbial-Mediated Processes. In *Combined Application of Physico-Chemical & Microbiological Processes for Industrial Effluent Treatment Plant*; Shah, M.; Banerjee, A., Eds.; Springer Singapore: Singapore, 2020; pp. 145−185, DOI: 10.1007/978-981-15-0497-6_8.

(7) Baeten, J. A Century of Red Water: Mine Waste, Legacy Contamination, and Institutional Amnesia in Minnesota's Mesabi Iron Range. *Water Hist.* **2018**, *10*, 245−266.

(8) Acharya, B. S.; Kharel, G. Acid Mine Drainage from Coal Mining in the United States − An Overview. *J. Hydrol.* **2020**, *588*, No. 125061.

(9) Leblanc, M.; Morales, J. A.; Borrego, J. 4,500-year-old Mining Pollution in Southwestern Spain: Long-Term Implications for Modern Mining Pollution. *Econ. Geol.* **2000**, *95*, 655−662.

(10) De Vleeschouwer, F.; Gérard, L.; Goormaghtigh, C.; Mattielli, N.; Le Roux, G.; Fagel, N. Atmospheric Lead and Heavy Metal Pollution Records from a Belgian Peat Bog Spanning the Last Two Millenia: Human Impact on a Regional to Global Scale. *Sci. Total Environ.* **2007**, *377*, 282−295.

(11) Machemer, S. D.; Reynolds, J. S.; Laudon, L. S.; Wildeman, T. R. *Balance of S in a Constructed Wetland Built to Treat Acid Mine Drainage*; Applied Geochemistry: Idaho Springs, Colorado, U.S.A. 1993, *8* (6), 587−603, DOI: 10.1016/0883-2927(93)90015-9.

(12) Blowes, D. W.; Ptacek, C. J.; Jambor, J. L.; Weisener, C. G.; Paktunc, D.; Gould, W. D.; Johnson, D. B. The Geochemistry of Acid Mine Drainage. In *Treatise on Geochemistry*; Elsevier, 2014; pp. 131−190, DOI: 10.1016/B978-0-08-095975-7.00905-0.

(13) Nordstrom, D. K.; Alpers, C. N. Geochemistry of Acid Mine Waters. In *The Environmental Geochemistry of Mineral Deposits*; 1999; p 29.

(14) Nordstrom, D. K.; Alpers, C. N.; Ptacek, C. J.; Blowes, D. W. Negative PH and Extremely Acidic Mine Waters from Iron Mountain, California. *Environ. Sci. Technol.* **2000**, *34*, 254−258.

(15) Sun, H.; Shi, B.; Yang, F.; Wang, D. Effects of Sulfate on Heavy Metal Release from Iron Corrosion Scales in Drinking Water Distribution System. *Water Res.* **2017**, *114*, 69−77.

(16) Taylor, J.; Pape, S.; Murphy, N. A Summary of Passive and Active Treatment Technologies for Acid and Metalliferous Drainage (AMD). In *Proceedings of the 5th Australian workshop on acid drainage*; 2005, 49.

(17) Sheoran, A. S.; Sheoran, V. Heavy Metal Removal Mechanism of Acid Mine Drainage in Wetlands: A Critical Review. *Miner. Eng.* **2006**, *19*, 105−116.

(18) Elliott, P.; Ragusa, S.; Catcheside, D. Growth of Sulfate-Reducing Bacteria under Acidic Conditions in an Upflow Anaerobic Bioreactor as a Treatment System for Acid Mine Drainage. *Water Res.* **1998**, *32*, 3724−3730.

(19) Utgikar, V. P.; Harmon, S. M.; Chaudhary, N.; Tabak, H. H.; Govind, R.; Haines, J. R. Inhibition of Sulfate-Reducing Bacteria by

Metal Sulfide Formation in Bioremediation of Acid Mine Drainage. *Environ. Toxicol.* **2002**, *17*, 40−48.
(20) *2018 Edition of the Drinking Water Standards and Health Advisories Tables*; U.S. Environmental Protection Agency: Washington, D.C., 2018.
(21) *Water Quality Standards for the Protection of Waters of the State*; Waters of the State; Minnesota Pollution Control Agency: Minnesota, 2020; p 221.
(22) LaFond-Hudson, S.; Johnson, N. W.; Pastor, J.; Dewey, B. Iron Sulfide Formation on Root Surfaces Controlled by the Life Cycle of Wild Rice (Zizania Palustris). *Biogeochemistry* **2018**, *141*, 95−106.
(23) *White Pine Treaty of 1837*; 1837.
(24) *1854 Treaty Authority*; 1854.
(25) Baeten, J.; Langston, N.; Lafreniere, D. A Spatial Evaluation of Historic Iron Mining Impacts on Current Impaired Waters in Lake Superior's Mesabi Range. *Ambio* **2018**, *47*, 231−244.
(26) Wilburn, D. R.; Bleiwas, D. I. *Platinum-Group Metals - World Supply and Demand*; Open-File Report; Open-File Report 2004−1224; United States Geological Survey, 2005; p 152.
(27) *Final Environmental Impact Statement (FEIS) NorthMet Mining Project and Land Exchange*. 3576.
(28) Peša, I.; Ross, C. Extractive Industries and the Environment: Production, Pollution, and Protest in Global History. *Extr. Ind. Soc.* **2021**, *8*, No. 100933.
(29) *A Federal Strategy to Ensure Secure and Reliable Supplies of Critical Minerals*; 2017, 60835−60837. https://www.govinfo.gov/content/pkg/FR-2017-12-26/pdf/2017-27899.pdf.
(30) *America's Supply Chains*; 2021, 11849−11854.
(31) *Minerals, Critical Minerals, and the U.S. Economy*; National Academies Press: Washington, D.C., 2008; p 12034, DOI: 10.17226/12034.
(32) Hao, T.; Xiang, P.; Mackey, H. R.; Chi, K.; Lu, H.; Chui, H.; van Loosdrecht, M. C. M.; Chen, G.-H. A Review of Biological Sulfate Conversions in Wastewater Treatment. *Water Res.* **2014**, *65*, 1−21.
(33) Zhang, L.; De Schryver, P.; De Gusseme, B.; De Muynck, W.; Boon, N.; Verstraete, W. Chemical and Biological Technologies for Hydrogen Sulfide Emission Control in Sewer Systems: A Review. *Water Res.* **2008**, *42*, 1−12.
(34) Pikaar, I.; Rozendal, R. A.; Yuan, Z.; Keller, J.; Rabaey, K. Electrochemical Sulfide Oxidation from Domestic Wastewater Using Mixed Metal-Coated Titanium Electrodes. *Water Res.* **2011**, *45*, 5381−5388.
(35) Jiang, G.; Sharma, K. R.; Guisasola, A.; Keller, J.; Yuan, Z. Sulfur Transformation in Rising Main Sewers Receiving Nitrate Dosage. *Water Res.* **2009**, *43*, 4430−4440.
(36) Jiang, F.; Liang, Z.-S.; Peng, G.-L.; Qian, J.; Chen, G.-H. Nitrogen Removal Capacity of Simultaneously Autotrophic and Heterotrophic Denitrification in a Sewer Receiving Nitrified Source-Separated Urine. *Water Pract. Technol.* **2013**, *8*, 33−40.
(37) Amos, R. T.; Mayer, K. U.; Blowes, D. W.; Ptacek, C. J. Reactive Transport Modeling of Column Experiments for the Remediation of Acid Mine Drainage. *Environ. Sci. Technol.* **2004**, *38*, 3131−3138.
(38) Bilek, F.; Wagner, S. Long Term Performance of an AMD Treatment Bioreactor Using Chemolithoautotrophic Sulfate Reduction and Ferrous Iron Precipitation under in Situ Groundwater Conditions. *Bioresour. Technol.* **2012**, *104*, 221−227.
(39) Dunnington, L. *Geothermal Heat for Remote Acid Mine Drainage Remediation: A Laboratory and Modelling Study*; Dissertation, Colorado School of Mines, Golden, CO, 2018.
(40) Habeeb, O. A.; Kanthasamy, R.; Saber, S. E. M.; Olalere, O. A. Characterization of Agriculture Wastes Based Activated Carbon for Removal of Hydrogen Sulfide from Petroleum Refinery Waste Water. *Mater. Today: Proc.* **2020**, *20*, 588−594.
(41) Shang, G.; Li, Q.; Liu, L.; Chen, P.; Huang, X. Adsorption of Hydrogen Sulfide by Biochars Derived from Pyrolysis of Different Agricultural/Forestry Wastes. *J. Air Waste Manage. Assoc.* **2016**, *66*, 8−16.
(42) Bagreev, A.; Bashkova, S.; Locke, D. C.; Bandosz, T. J. Sewage Sludge-Derived Materials as Efficient Adsorbents for Removal of Hydrogen Sulfide. *Environ. Sci. Technol.* **2001**, *35*, 1537−1543.
(43) Awe, O. W.; Minh, D. P.; Lyczko, N.; Nzihou, A.; Zhao, Y. Laboratory-Scale Investigation of the Removal of Hydrogen Sulfide from Biogas and Air Using Industrial Waste-Based Sorbents. *J. Environ. Chem. Eng.* **2017**, *5*, 1809−1820.
(44) Kinnunen, P. H.-M.; Kaksonen, A. H. Towards Circular Economy in Mining: Opportunities and Bottlenecks for Tailings Valorization. *J. Cleaner Prod.* **2019**, *228*, 153−160.
(45) Savini, F. The Economy That Runs on Waste: Accumulation in the Circular City. *J. Environ. Policy Plann.* **2019**, *21*, 675−691.
(46) Swain, B.; Lee, C. G. Commercial Indium Recovery Processes Development from Various E-(Industry) Waste through the Insightful Integration of Valorization Processes: A Perspective. *Waste Manage.* **2019**, *87*, 597−611.
(47) Zanko, L. M.; Fosnacht, D. R.; Hopstock, D. M. Construction Aggregate Potential of Minnesota Taconite Industry Byproducts. In *Cold Regions Engineering 2009*; American Society of Civil Engineers: Duluth, Minnesota, United States, 2009; pp. 252−274, DOI: 10.1061/41072(359)27.
(48) *NRRI Semi-Annual Report: January−June*; Natural Resources Research Institute: Duluth, Minnesota, United States, 2013; pp. 4, 43.
(49) Voelz, J. L.-A. *Classifying Iron in Redox Reactions between Iron-Bearing Minerals and Environmental Contaminants*; University of Minnesota: Minneapolis, MN, 2019.
(50) Anastas, P.; Eghbali, N. Green Chemistry: Principles and Practice. *Chem. Soc. Rev.* **2010**, *39*, 301−312.
(51) Seager, T.; Selinger, E.; Wiek, A. Sustainable Engineering Science for Resolving Wicked Problems. *J. Agric. Environ. Ethics* **2012**, *25*, 467−484.
(52) Tayebi-Khorami, M.; Edraki, M.; Corder, G.; Golev, A. Re-Thinking Mining Waste through an Integrative Approach Led by Circular Economy Aspirations. *Minerals* **2019**, *9*, 286.
(53) Izevbekhai, B.; Rohne, R. *MnROAD Cell 54: Cell Constructed With Mesabi-Select (Taconite-Overburden) Aggregate; Construction and Early Performance*; 2008.
(54) Rickard, D. *Sulfidic Sediments and Sedimentary Rocks*; Developments in Sedimentology; Elsevier, 2012; Vol. 65.
(55) Wan, M.; Shchukarev, A.; Lohmayer, R.; Planer-Friedrich, B.; Peiffer, S. Occurrence of Surface Polysulfides during the Interaction between Ferric (Hydr)Oxides and Aqueous Sulfide. *Environ. Sci. Technol.* **2014**, *48*, 5076−5084.
(56) Peiffer, S.; Behrends, T.; Hellige, K.; Larese-Casanova, P.; Wan, M.; Pollok, K. Pyrite Formation and Mineral Transformation Pathways upon Sulfidation of Ferric Hydroxides Depend on Mineral Type and Sulfide Concentration. *Chem. Geol.* **2015**, *400*, 44−55.
(57) Wan, M.; Schröder, C.; Peiffer, S. Fe(III):S(-II) Concentration Ratio Controls the Pathway and the Kinetics of Pyrite Formation during Sulfidation of Ferric Hydroxides. *Geochim. Cosmochim. Acta* **2017**, *217*, 334−348.
(58) Rickard, D. T. Synthesis of Smythite - Rhombohedral Fe3S4. *Nature* **1968**, *218*, 356−357.
(59) Furukawa, Y.; Barnes, H. L. Reactions Forming Smythite, Fe9S11. *Geochim. Cosmochim. Acta* **1996**, *60*, 3581−3591.
(60) Kaksonen, A. H.; Riekkola-Vanhanen, M.-L.; Puhakka, J. A. Optimization of Metal Sulphide Precipitation in Fluidized-Bed Treatment of Acidic Wastewater. *Water Res.* **2003**, *37*, 255−266.
(61) Daire, J. *Evolving Reactivity and Products of Natural Iron- Bearing Minerals toward Sulfide*; University of Minnesota: Duluth, MN, 2019.
(62) Nesic, S.; Sun, W. Corrosion in Acid Gas Solutions. In *Shreir's Corrosion*; Elsevier: Oxford, 2010; pp. 1270−1298, DOI: 10.1016/B978-044452787-5.00055-X.
(63) Sun, W.; Nesic, S. 07655 - A Mechanistic Model of H2S Corrosion of Mild Steel. In *Corrosion*; OnePetro, 2007.
(64) Smith, S. N.; Sun, W. 11081: Corrosion at Higher H2S Concentrations and Moderate Temperatures. In *Corrosion*; OnePetro, 2011.

(65) Sun, W. *Kinetics of Iron Carbonate and Iron Sulfide Scale Formation in CO2/H2S Corrosion*; Ohio University: Athens, Ohio, 2006.
(66) Smith, J. S.; Miller, J. D. A. Nature of Sulphides and Their Corrosive Effect on Ferrous Metals: A Review. *Br. Corros. J.* **1975**, *10*, 136−143.
(67) Mangayayam, M. C.; Perez, J. P. H.; Dideriksen, K.; Freeman, H. M.; Bovet, N.; Benning, L. G.; Tobler, D. J. Structural Transformation of Sulfidized Zerovalent Iron and Its Impact on Long-Term Reactivity. *Environ. Sci.: Nano* **2019**, *6*, 3422−3430.
(68) Sánchez-Andrea, I.; Sanz, J. L.; Bijmans, M. F. M.; Stams, A. J. M. Sulfate Reduction at Low PH to Remediate Acid Mine Drainage. *J. Hazard. Mater.* **2014**, *269*, 98−109.
(69) Ňancucheo, I.; Johnson, D. B. Selective Removal of Transition Metals from Acidic Mine Waters by Novel Consortia of Acidophilic Sulfidogenic Bacteria. *Microb. Biotechnol.* **2012**, *5*, 34−44.
(70) Kolmert, A.; Johnson, D. B. Remediation of Acidic Waste Waters Using Immobilised, Acidophilic Sulfate-Reducing Bacteria. *J. Chem. Technol. Biotechnol.* **2001**, *76*, 836−843.
(71) Soroush, A.; Penn, R. L.; Arnold, W. A. Anisotropic Oxidative Growth of Goethite-Coated Sand Particles in Column Reactors during 4-Chloronitrobenzene Reduction by Fe(II)/Goethite. *Environ. Sci.: Nano* **2022**, *9*, 275−288.
(72) Dev, S.; Galey, M.; Chun, C. L.; Novotny, C.; Ghosh, T.; Aggarwal, S. Enrichment of Psychrophilic and Acidophilic Sulfate-Reducing Bacterial Consortia − a Solution toward Acid Mine Drainage Treatment in Cold Regions. *Environ. Sci.: Processes Impacts* **2021**, *23*, 2007−2020.
(73) Muyzer, G.; Stams, A. J. M. The Ecology and Biotechnology of Sulphate-Reducing Bacteria. *Nat. Rev. Microbiol.* **2008**, *6*, 441−454.
(74) Di Toro, D. M.; Mahony, J. D.; Hansen, D. J.; Scott, K. J.; Hicks, M. B.; Mayr, S. M.; Redmond, M. S. Toxicity of Cadmium in Sediments: The Role of Acid Volatile Sulfide. *Environ. Toxicol. Chem.* **1990**, *9*, 1487−1502.
(75) Viollier, E.; Inglett, P. W.; Hunter, K.; Roychoudhury, A. N.; Van Cappellen, P. The Ferrozine Method Revisited: Fe(II)/Fe(III) Determination in Natural Waters. *Appl. Geochem.* **2000**, *15*, 785−790.
(76) US EPA Methylene Blue Method.Pdf.
(77) Schneider, C. A.; Rasband, W. S.; Eliceiri, K. W. NIH Image to ImageJ: 25 Years of Image Analysis. *Nat. Methods* **2012**, *9*, 671−675.
(78) Rickard, D.; Luther, G. W. Chemistry of Iron Sulfides. *Chem. Rev.* **2007**, *107*, 514−562.
(79) Morse, J. W.; Millero, F. J.; Cornwell, J. C.; Rickard, D. The Chemistry of the Hydrogen Sulfide and Iron Sulfide Systems in Natural Waters. *Earth-Sci. Rev.* **1987**, *24*, 1−42.
(80) Bush, R. T.; Fyfe, D.; Sullivan, L. A. Occurrence and Abundance of Monosulfidic Black Ooze in Coastal Acid Sulfate Soil Landscapes. *Soil Res.* **2004**, *42*, 609.
(81) Wei, D.; Osseo-Asare, K. Formation of Iron Monosulfide: A Spectrophotometric Study of the Reaction between Ferrous and Sulfide Ions in Aqueous Solutions. *J. Colloid Interface Sci.* **1995**, *174*, 273−282.
(82) Matamoros-Veloza, A.; Stawski, T. M.; Benning, L. G. Nanoparticle Assembly Leads to Mackinawite Formation. *Cryst. Growth Des.* **2018**, *18*, 6757−6764.
(83) Bénézeth, P.; Dandurand, J. L.; Harrichoury, J. C. Solubility Product of Siderite (FeCO3) as a Function of Temperature (25−250 °C). *Chem. Geol.* **2009**, *265*, 3−12.
(84) Pohl, H. A. Solubility of Iron Sulfides. *J. Chem. Eng. Data* **1962**, *7*, 295−306.
(85) Rickard, D. The Solubility of FeS. *Geochim. Cosmochim. Acta* **2006**, *70*, 5779−5789.
(86) Liu, Y.; Zhang, Z.; Bhandari, N.; Dai, Z.; Yan, F.; Ruan, G.; Lu, A. Y.; Deng, G.; Zhang, F.; Al-Saiari, H.; Kan, A. T.; Tomson, M. B. New Approach to Study Iron Sulfide Precipitation Kinetics, Solubility, and Phase Transformation. *Ind. Eng. Chem. Res.* **2017**, *56*, 9016−9027.
(87) Sparks, D. L. Kinetics of Soil Chemical Processes. In *Environmental Soil Chemistry*; Academic Press, 2003; pp. 207−244.
(88) *Kinetics of Water-Rock Interaction*; Brantley, S. L.; Kubicki, J. D.; White, A. F., Eds.; Springer Verlag: New York, 2008.
(89) Graham, A.; Salleh, I.; Ibrahim, J.; Khairuddin, K.; Singleton, M.; Sorbie, K. An Experimental Determination of Hydrogen Sulfide Scavenging Capacities and Mechanisms in Iron-Bearing Minerals. In *SPE International Oilfield Scale Conference and Exhibition*; Society of Petroleum Engineers: Virtual, 2020, DOI: 10.2118/200677-MS.
(90) Bourdoiseau, J.-A.; Jeannin, M.; Rémazeilles, C.; Sabot, R.; Refait, P. The Transformation of Mackinawite into Greigite Studied by Raman Spectroscopy. *J. Raman Spectrosc.* **2011**, *42*, 496−504.
(91) Lennie, A. R.; Redfern, S. A. T.; Champness, P. E.; Stoddart, C. P.; Schofield, P. F.; Vaughan, D. J. Transformation of Mackinawite to Greigite; an in Situ X-Ray Powder Diffraction and Transmission Electron Microscope Study. *Am. Mineral.* **1997**, *82*, 302−309.
(92) Moon, E. M.; Bush, R. T.; Gibbs, D. H. M.; Mata, J. P. Divergent Fe and S Mineralization Pathways during the Oxidative Transformation of Greigite, Fe3S4. *Chem. Geol.* **2017**, *468*, 42−48.
(93) Benning, L. G.; Wilkin, R. T.; Barnes, H. L. Reaction Pathways in the Fe−S System below 100°C. *Chem. Geol.* **2000**, *167*, 25−51.
(94) Mozley, P. S. Relation between Depositional Environment and the Elemental Composition of Early Diagenetic Siderite. *Geologija* **1989**, *17*, 704.
(95) Kanaya, K. A.; Okayama, S. Penetration and Energy-Loss Theory of Electrons in Solid Targets. *J. Phys. D: Appl. Phys.* **1972**, *5*, 43−58.
(96) Wolthers, M.; Van der Gaast, S. J.; Rickard, D. The Structure of Disordered Mackinawite. *Am. Mineral.* **2003**, *88*, 2007−2015.
(97) Muñoz-Santiburcio, D.; Wittekindt, C.; Marx, D. Nanoconfinement Effects on Hydrated Excess Protons in Layered Materials. *Nat. Commun.* **2013**, *4*, 2349.
(98) Beauvais, M. L.; Chupas, P. J.; O'Nolan, D.; Parise, J. B.; Chapman, K. W. Resolving Single-Layer Nanosheets as Short-Lived Intermediates in the Solution Synthesis of FeS. *ACS Mater. Lett.* **2021**, *3*, 698−703.
(99) Saeed Akhtar, M.; Alenad, A.; Azad Malik, M. Synthesis of Mackinawite FeS Thin Films from Acidic Chemical Baths. *Mater. Sci. Semicond. Process.* **2015**, *32*, 1−5.
(100) Csákberényi-Malasics, D.; Rodriguez-Blanco, J. D.; Kis, V. K.; Rečnik, A.; Benning, L. G.; Pósfai, M. Structural Properties and Transformations of Precipitated FeS. *Chem. Geol.* **2012**, *294-295*, 249−258.
(101) Matamoros-Veloza, A.; Cespedes, O.; Johnson, B. R. G.; Stawski, T. M.; Terranova, U.; de Leeuw, N. H.; Benning, L. G. A Highly Reactive Precursor in the Iron Sulfide System. *Nat. Commun.* **2018**, *9*, 3125.
(102) Shoesmith, D. W.; Taylor, P.; Bailey, M. G.; Owen, D. G. The Formation of Ferrous Monosulfide Polymorphs during the Corrosion of Iron by Aqueous Hydrogen Sulfide at 21°C. *J. Electrochem. Soc.* **1980**, *127*, 1007−1015.
(103) Wen, X.; Bai, P.; Luo, B.; Zheng, S.; Chen, C. Review of Recent Progress in the Study of Corrosion Products of Steels in a Hydrogen Sulphide Environment. *Corros. Sci.* **2018**, *139*, 124−140.
(104) Smith, S. N. Current Understanding of Corrosion Mechanisms Due to H2S in Oil and Gas Production Environments. In *NACE International*; NACE International: Houston, TX, 2015; p 18.
(105) Schippers, A.; Sand, W. Bacterial Leaching of Metal Sulfides Proceeds by Two Indirect Mechanisms via Thiosulfate or via Polysulfides and Sulfur. *Appl. Environ. Microbiol.* **1999**, *65*, 319−321.
(106) Schoenberger, E. Environmentally Sustainable Mining: The Case of Tailings Storage Facilities. *Resour. Policy* **2016**, *49*, 119−128.
(107) Vigneault, B. Geochemical Changes in Sulfidic Mine Tailings Stored under a Shallow Water Cover. *Water Res.* **2001**, *35*, 1066−1076.
(108) Ahmed, S. M. Surface Chemical Methods of Forming Hardpan in Pyrrhotite Tailings and Prevention of the Acid Mine Drainage. *ASMR* **1994**, *1994*, 57−66.

(109) Waybrant, K. R.; Ptacek, C. J.; Blowes, D. W. Treatment of Mine Drainage Using Permeable Reactive Barriers: Column Experiments. *Environ. Sci. Technol.* **2002**, *36*, 1349−1356.

https://doi.org/10.1021/acsearthspacechem.3c00080
ACS Earth Space Chem. 2023, 7, 1247−1257